Tellus (1993), 45A, 408–423
Printed in Belgium – all rights reserved

TELLUS
ISSN 0280–6495

The dynamics of error covariances in a barotropic model

By FRANÇOIS BOUTTIER, *Météo-France/CNRM, 42 Av. Coriolis, 31057 Toulouse, France*

(Manuscript received 2 November 1992; in final form 25 February 1993)

ABSTRACT

Under the hypothesis of linear error growth, the tangent linear model can be used to provide a simplified form of stochastic-dynamic prediction, in which the uncertainty on a model forecast is defined by the error covariances between the model state variables. We apply this method on a global vorticity equation model with a simple initial condition for the covariance matrix. The forecast error variances and correlations undergo rapid modifications in relation with the atmospheric flow pattern. This may have some implications for operational assimilation schemes in numerical weather prediction. A deeper understanding of the relevant processes is sought, using an adjoint form of the prediction equation, in order to assess the impact of the initial variances and correlations, and of the intrinsic dynamics of the model flow. The application on some simplified flows shows the relevance of diffusion, advection, Rossby wave dispersion and barotropic instability to forecast skill prediction.

1. Introduction

Weather forecasts are inevitably uncertain. The reason is that the present state of the atmosphere is only approximately known, and predicting its time evolution involves some additional errors because numerical weather models are not a perfect representation of the reality. Moreover, error may increase with time because of the unstable nature of atmospheric flow dynamics. As a consequence, the probabilistic nature of atmospheric model forecasts has to be explicitly taken into account for estimating the initial state in numerical weather prediction. This idea forms the basis for most modern objective analysis methods (Lorenc, 1986; Ghil, 1989). One of them is optimal interpolation, which is usually used for operational systems, and requires the specification of the error covariances of the guess field. This specification is commonly achieved empirically following statistical studies (Hollingsworth and Lönnberg, 1986; Lönnberg and Hollingsworth, 1986), although it is theoretically possible to obtain optimal estimations of those statistics from the integration of the corresponding Kalman filter (Ghil et al., 1981). Several attempts have been made to include probabilistic information into the forecast itself (Epstein, 1969). The interest in this formalism has been growing in past years, as the improvement of operational models at the short and medium range is demonstrating the potential value of a forecast of forecast skill (Palmer and Tibaldi, 1987; Barkmeijer and Opsteegh, 1991; Veyre, 1991).

The first step for including probabilistic information into a deterministic prediction is to compute the second-order moments of the probability density function of the atmospheric state. In a discrete framework, this takes the form of an error covariance matrix, the size of which is the square of the dimension of the model state variable. If the evolution of errors can be approximated by the tangent linear of the model, an assumption which holds at least at short ranges for the large scale, upper level dynamics (Lacarra and Talagrand, 1988; Veyre, 1991), then the error covariance matrix evolves according to a simple deterministic equation. Although this prediction equation is well known, it has been integrated only in very simplified conditions (Ghil et al., 1981; Cohn and Parrish, 1991), so that its physical behaviour in meteorological models is badly understood. A reason is the enormous computational cost involved, which is in fact the main stumbling block for practical implementation of the Kalman filter in numerical models. On the other hand, it is believed that the integration of the error covariances, at least in a degraded form, could improve the optimal interpolation, and provide some useful information for short-range forecast of forecast skill. This is conceivable only if numerically cheap integration methods are found. Some work has been done in this field (Parrish and Cohn, 1985; Dee, 1991), but the results have to be extended to more realistic situations. In particular, it is certainly important to take into account the error growth processes in relation with hydrodynamic instabilities.

This study is expected to provide a better physical understanding of the behaviour of forecast error covariances, with emphasis on the effects of the flow dynamics. It is a first step towards designing physically sound simplifications of covariances prediction for practical uses. Additionally, one may gain a better knowledge on the predictability of the real atmosphere, if the methodology presented here is extended to more realistic models. The derivation of the equation and a short discussion of its technical implementation are given in Section 2. As a first step, an error matrix prediction experiment is presented in Section 3, with a very simple initial condition, to show the challenging nature of the relations between dynamics and error covariances evolution. It is necessary to transform the prediction equation in order to facilitate the interpretation of the former results. This is done in Section 4, and applied to simple flows in Section 5. The results are discussed in Section 6.

2. The prediction of error covariances

The use of the tangent linear equations first requires the definition of the reference trajectory with respect to which the model is linearized. In this paper, it is given as the integration of the barotropic vorticity equation on the sphere, with a small diffusion, starting from a pre-defined initial condition. The spectral model is discretized using a triangular spectral truncation at total wavenumber 21. All computations presented in this paper have been achieved using the ARPEGE/IFS code (Courtier et al., 1991). In most experiments presented here, the integration time is 24 h. Several authors (Lacarra and Talagrand, 1988; Veyre, 1991) have shown that the evolution of synoptic-scale features of 500 hPa height analysis errors in such a model is satisfactorily linear for up to 48 h at least. Hence, we expect the evolution of analysis errors, relative to the reference trajectory, to be accurately predicted by the tangent linear of the vorticity equation model:

$$\varepsilon_t = R\varepsilon_0 \tag{1}$$

where R is the resolvent of tangent linear model between times 0 and t, ε_0 is a model state vector representing an analysis error field and ε_t is the subsequent forecast error. Assuming the analysis error matrix P_0 is known, the corresponding forecast error matrix P_t is obtained by multiplying the above equation by its transpose (denoted by the superscript T) and taking the ensemble mean $\langle\,.\,\rangle$ of the result:

$$\langle \varepsilon_t \varepsilon_t^{\mathrm{T}} \rangle = \langle R\varepsilon_0 \varepsilon_0^{\mathrm{T}} R^{\mathrm{T}} \rangle. \tag{2}$$

Assuming R is exactly known yields, by linearity,

$$P_t = RP_0R^{\mathrm{T}}. \tag{3}$$

Eq. (3) is the prediction equation for the error covariances. If one does not assume that R is exactly known, a "model" noise covariance matrix has to be added at each timestep on its right-hand side to account for model errors. How such a matrix should be specified is yet unclear; some simple forms are tested in Pitcher (1977) and Cohn and Parrish (1991). Keeping in mind that model error noise will have to be accounted for in operational applications, it has been decided to neglect it in this exploratory study in order to concentrate on the specific effects of the model dynamics.

The dimension of the model variable state is $n = 483$. It is several orders of magnitude larger in current operational models. The evaluation of P_t requires $2n$ integrations of the tangent linear model, since eq. (3) is equivalent to

$$P_t = R(RP_0)^{\mathrm{T}} \tag{4}$$

(P_0 and P_t are symmetric positive matrices). This computational cost may be reduced to n if the coefficients of the resolvent R are computed and stored as an explicit matrix, so that the remaining operations reduce to matrix multiplications. On the other hand, the handling of such matrices requires the storage of $n \times n$ coefficients ($n(n+1)/2$ for a

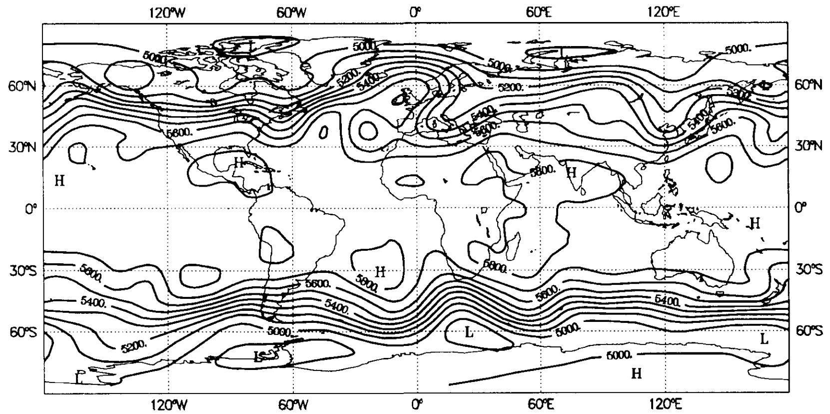

Fig. 1. 500 hPa geopotential height analysis from ECMWF, on 1 December 1990, 00 UTC, at T21 triangular spectral truncation, in meters.

symmetric matrix). Thus it is evident that both numerical costs and memory requirements will be prohibitive for the evaluation of P_t in higher resolution models. From the point of view of Dee (1991), there is simply not enough information available in practice to provide such a large amount of statistics as is contained in P_0. On the other hand, it is possible that the model dynamics are able to feed valuable information into P_t, so that the huge numerical cost involved may be at least partially justified. As described in the following section, an explicit integration of (3) gives indications that there is indeed some interesting information in P_t.

3. An example of error covariance prediction

In this section, a reference trajectory is built using the 24-h vorticity equation model prediction starting from the 500 hPa height field shown in Fig. 1, which is the T21 filtered ECMWF analysis for the 1 December 1989, 00 UTC. The corresponding vorticity field is computed using a linear balance equation. The 500 hPa height 24-h forecast is fair when compared with the corresponding analysis. The initial error condition P_0 has been purposely taken as very simple: the height covariance between two points i and j is given by

$$\mathrm{cov}(i, j) = \sigma_z^a(i)\, \sigma_z^a(j)\, \mathrm{e}^{-d(i,j)^2/(2d^2)}, \tag{5}$$

where $d(i, j)$ is the distance on the sphere between i and j, $a = 565$ km and $\sigma_z^a(k)$ is a r.m.s. error field depending only on the latitude of the point k: it is specified analytically with constant values far from the equator in each hemisphere, a slightly higher value in the southern hemisphere to account for higher analysis errors, and reduced values in low

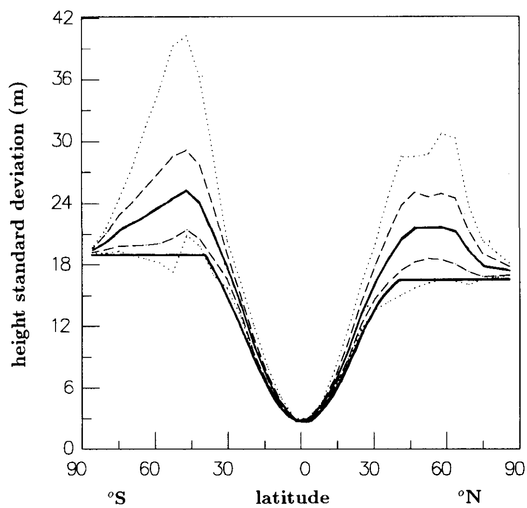

Fig. 2. Zonal-mean repartition of initial and forecast height error standard deviation, in meters, for the first experiment. Lower heavy curve: initial condition; Higher heavy curve: zonal mean of the 24-h forecast. The dashed lines and dotted lines indicate, respectively, the standard deviation and the extrema for each latitude.

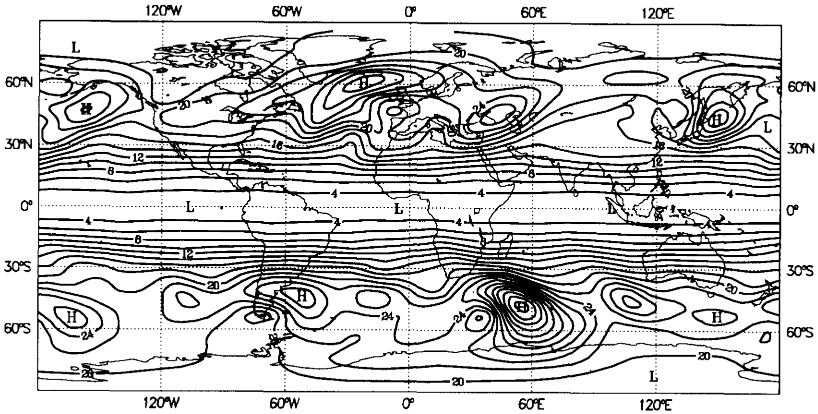

Fig. 3. Forecast height error standard deviation (m) in the first experiment.

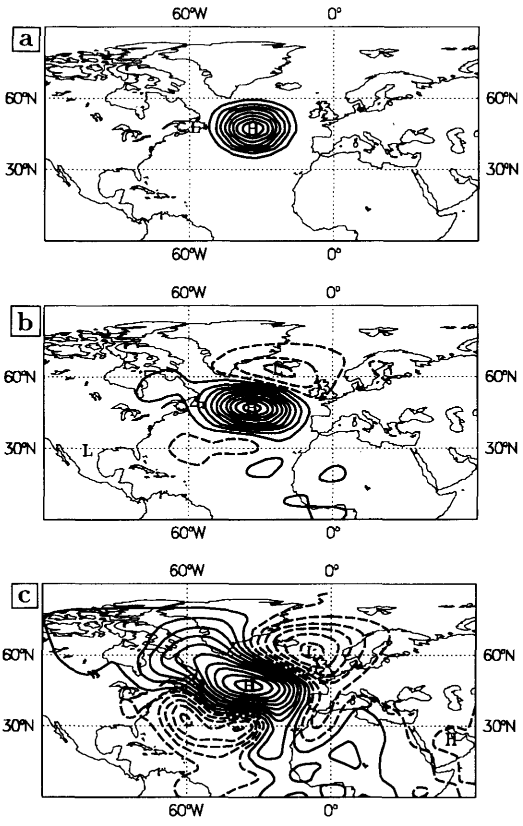

Fig. 4. Evolution of the height autocorrelation field relative to the point at (45° N, 35° W), in the first experiment. (a) initial state: (b) 6-h forecast; (c) 24-h forecast. The interval is 0.1, while the highest isoline at 0.95.

latitudes so that the vorticity errors remain reasonable when using the geostrophic assumption near the equator. The dependence of σ_z^a with latitude is shown by the lower curve in Fig. 2. The square root of the diagonal of an error covariance matrix in physical space is equivalent to a r.m.s. error field, i.e., the geographical repartition of the uncertainty on the model state. In P_0, it is equal to the σ_z^a field. Its counterpart in the forecast matrix P_t is shown in Fig. 3: the zonal symmetry of the initial matrix is lost due to the model dynamics. The zonal mean of this field, and the departures from the zonal mean are shown in Fig. 2. While the uncertainty remains almost unchanged between the tropics, there is a significant increase in mid-latitudes where the dynamics are particularly active. Decreases of the r.m.s. errors are rare and do not seem to be significant. The largest increases are concentrated in small areas and amount to a doubling of the initial error in 24 h. The larger the forecast r.m.s. error, the smaller the atmospheric predictability, so that one would expect larger prediction errors in such cases. This property has been verified statistically by previous works with slightly different methods (Veyre, 1991; Barkmeijer and Opsteegh, 1992). A comparison between Fig. 1 and Fig. 3 does not reveal any general rule for associating high forecast r.m.s. errors (or, equivalently, error variances) with a particular flow pattern. One may just state that higher variances tend to be located on the eastern flank of large-scale troughs and in the outlet of strong jets. Actually, these qualitative characteristics hold approximately when the experiment is carried out with other trajectories, starting from analyses on several days.

Another outstanding feature of the error matrix evolution is the deformation of the correlation patterns. It is important to remember that a covariance error matrix contains much more information than is apparent in its diagonal, because it defines a joint probability distribution between all parameters of the model. The non-diagonal terms represent probabilistic relationships between these parameters. The link between the prediction (or the analysis) of a parameter on a point, called the reference point, and the prediction of the same parameter on the rest of the model grid is accurately represented by the horizontal autocorrelation field, which shows the covariances with that point, normalized by the corresponding standard deviations. To illustrate this, an arbitrary reference point has been chosen at (45° N, 35° W); the panel (a) of Fig. 4 shows the corresponding autocorrelation field in the initial matrix P_0, for the 500 hPa height. Following the analytic specification of the correlation model, it takes the form of an isotropic gaussian, with a maximum of 1 at the reference point (the small anisotropy on the map is related to the operation of projecting the sphere onto the plane). It means that the analysis errors on two points are positively correlated if, and only if, those points are closer than a typical influence radius of several hundred kilometers, i.e., the height analysis contains no error on a smaller scale. This assumption is often made in operational analysis processes. Panels (b) and (c) of Fig. 4 show the evolution of the autocorrelation after an integration of 6 h and 24 h, respectively, of the error matrix, using the same trajectory as before. After 6 h, the autocorrelation is neither isotropic, nor positive any more, since a significant lobe of down to -0.26 negative correlations appears northeast of the reference point. The "influence radius" changes, with significantly non-zero correlations extending further from the reference point than in the initial condition. After 24 h, these characteristics are even more marked, with a strong tripolar structure and negative correlations down to -0.56.

The examination of other autocorrelation fields show the same gross features, with a dependence of the shape on the trajectory flow characteristics. To get a global view of the predicted correlation structures, it is useful to characterize each autocorrelation field with a small number of scalar parameters representing the influence radius and the anisotropy. In conventional correlation models, the influence radius is computed as the distance at which the second derivative of the structure function vanishes. Following eq. (5), it is equal in P_0 to $a = 565$ km. In the predicted matrices, this definition loses its significance because the correlations are neither isotropic nor decreasing with distance. We are going to use

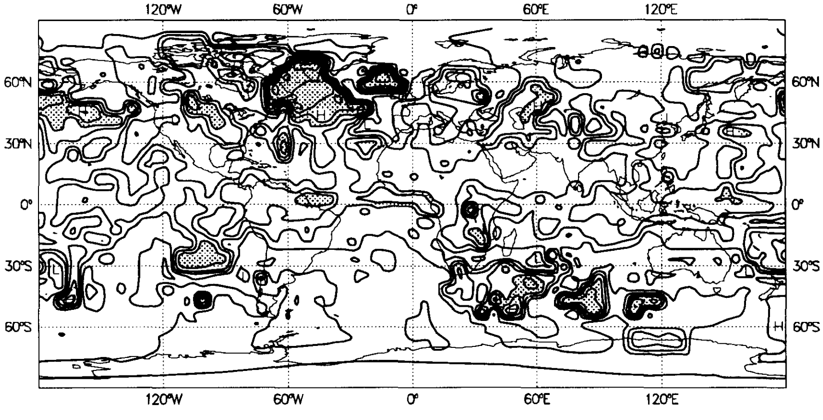

Fig. 5. Mapping of the maximum distance at which height correlations are greater than 0.15 in absolute value, in the 24-h forecast error matrix of the first experiment. The interval is $2 \cdot 10^6$ m and the hatched areas correspond to distances greater than 5000 km.

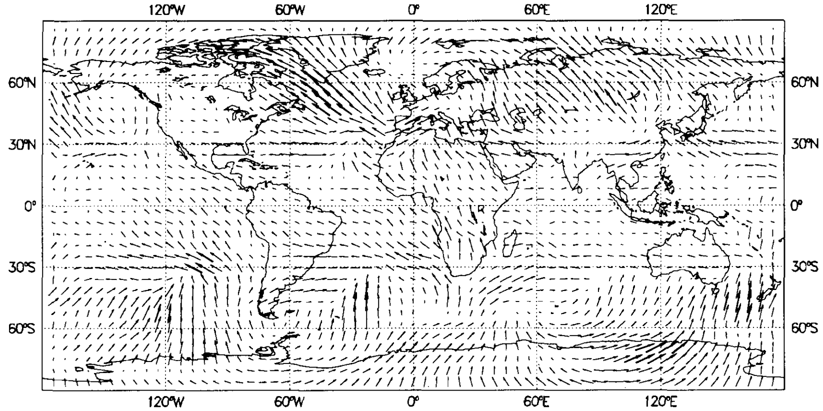

Fig. 6. Mapping of the anisotropy of the height autocorrelation fields in the forecast error matrix of the first experiment. The length of the arrows indicate the oblateness of the autocorrelation fields, their direction is that of the great axis of their inertia ellipsoid as defined in Section 3. The arrows are arbitrarily oriented northwards, their scaling is such that the largest one corresponds to an oblateness of 2.

another measure of the distance at which the correlations are significant: for each point, we define the influence distance as the maximum distance where some correlations are larger, in absolute value, than a given threshold. The mapping of this parameter is shown in Fig. 5, using a threshold of 0.15, with hatched areas highlighting areas of particularly large influence distance. The field is rather noisy, since the parameter is a non-linear function of the autocorrelation fields. On the average, it increases by a factor two in 24 h, with large local maxima, up to 8000 km. In the initial matrix P_0 it was uniformly equal to 1100 km, so that the matrix prediction processes involves a significant increase of the influence distance. The largest values are found in mid-latitudes, often (but not always) where the increase in standard deviation is the highest.

Another outstanding feature is the anisotropy of the correlations. It is neglected in most currently operational analysis procedures. It is defined at each point as follows: first, the autocorrelation field is mapped from the sphere to the tangent plane at that point, in such a way that there are almost no changes to the field geometry near the point, where the most significant correlations are usually found. Then, we compute the inertia matrix of this field $\rho(x, y)$ on the tangent plane:

$$\begin{bmatrix} \int \rho(x, y)\, x^2 \,\mathrm{d}x\, \mathrm{d}y & \int \rho(x, y)\, xy \,\mathrm{d}x\, \mathrm{d}y \\ \int \rho(x, y)\, xy \,\mathrm{d}x\, \mathrm{d}y & \int \rho(x, y)\, y^2 \,\mathrm{d}x\, \mathrm{d}y \end{bmatrix}.$$

All negative correlation values ρ are removed to ensure that the inertia matrix is positive definite. The eigenvectors of the matrix define the directions of the anisotropy, and the rate of the eigenvalues is a measure of the oblateness. These quantities do not depend on the choice of the local (x, y) framework used to compute the coefficients. The anisotropy of the correlation field is then summarized by a vector whose direction is that of the largest eigenvector, and the norm is the oblateness of the inertia ellipsoid minus one (so that the null vector corresponds to isotropy). The mapping of the vector on the globe is shown in Fig. 6. The maximum oblateness is equal to 2, corresponding to correlations extending typically twice as far in a direction as in the perpendicular. There is some regularity in the vector field, which was not an evident fact a priori. The largest vectors are found in the vicinity of the largest r.m.s. errors, indicating that there must be some connection between correlation anisotropy and strong error growth. Though it is hard to state anything general about the directions, one may say the correlations tend to extend NW-SE near the northern hemisphere jet, and NE-SW in the southern hemisphere.

This sample integration shows that, even in very simplified framework, the model dynamics are able to put a lot of information into the forecast error matrix. Unfortunately, the physical nature of this information is hard to understand because of the special form of the prediction eq. (3), in which the evolving variable, a covariance matrix, is very large, and the model dynamics appear twice as a tangent linear integration. It is possible to solve this difficulty by using a local form of the prediction equation, as demonstrated in the next section.

4. Decomposition of the forecast covariances

We note p_i the value of a scalar parameter i, for instance the 500 hPa height at one gridpoint. If i is linearly related to the model state vector X, then it is possible to define an operator H_i such that

$$p_i = H_i X, \tag{6}$$

which is simply a generalized form of interpolation: if i is the value of X at a point, H_i is a row matrix containing the coefficients of the interpolation on that point. When H_i is applied to an error field, it provides the corresponding error on the parameter i. The forecast error covariance between two parameters i and j is given by

$$\operatorname{cov}(i, j) = H_i P_t H_j^{\mathrm{T}} \tag{7}$$

$$= H_i R P_0 R^{\mathrm{T}} H_j^{\mathrm{T}} \tag{8}$$

$$= \langle R^{\mathrm{T}} H_i^{\mathrm{T}}, R^{\mathrm{T}} H_j^{\mathrm{T}} \rangle_{P_0}, \tag{9}$$

where $\langle .,. \rangle_{P_0}$ is the inner product defined by the matrix P_0. Thus, the dynamics relevant to one particular covariance are contained in only two adjoint integrations of the appropriate adjoint interpolators (H_i^{T}, H_j^{T}), while the useful probabilistic information takes the form of a particular quadratic form. The practical aspects of computing the adjoint interpolators are depicted in Gauthier et al. (1993). Computing one forecast error variance for a parameter i is even simpler, since it is given as cov(i, i) by one single adjoint integration to compute $R^{\mathrm{T}} H_i^{\mathrm{T}}$, and by some matrix multiplications (Opsteegh, personal communication).

It is interesting to interpret the effect of matrix P_0 in some details by separating the effects of the initial variance field and the correlations, following

$$P_0 = SCS, \tag{10}$$

where C is the initial correlation matrix, and S is a diagonal matrix whose coefficients are the square roots of the respective diagonal elements of P_0. The covariance prediction equation can be put in a completely symmetric form by factorizing C, which is positive definite, as

$$C = T^{\mathrm{T}} T, \tag{11}$$

where T is not necessarily triangular; it is not uniquely defined, either, since another factorization is given by $C = T^{\mathrm{T}} U^{\mathrm{T}} U T$, where U is any unitary matrix (i.e., $U^{\mathrm{T}} = U^{-1}$). It is then possible to get rid of the definition of a particular quadratic form:

$$\operatorname{cov}(i, j) = H_i R S T^{\mathrm{T}} T S R^{\mathrm{T}} H_j^{\mathrm{T}} \tag{12}$$

$$= \langle T S R^{\mathrm{T}} H_i^{\mathrm{T}}, T S R^{\mathrm{T}} H_j^{\mathrm{T}} \rangle, \tag{13}$$

where $\langle .,. \rangle$ is the canonical inner product. The prediction of one particular variance takes a sequential form:

$$\operatorname{cov}(i, i) = \| T S R^{\mathrm{T}} H_i^{\mathrm{T}} \|^2, \tag{14}$$

in which each operation may be readily interpreted with our simple initial condition P_0.

The so-called adjoint interpolator H_i^{T} depends only on the definition of i and on the model discretization. In the following, i will be the 500 hPa height at (45°N, 35°W). The corresponding H_i^{T} field in streamfunction space is the gradient of i with respect to the model state. It is almost isotropic around the (45°N, 35°W) point; it is equal to $0.24 \cdot 10^{-5}\ \mathrm{m}^{-1}\ \mathrm{s}$ on the point, and very close to zero at distances larger than 1500 km. It has been found that gradient fields are much easier to read in streamfunction than in geopotential height space, because the conversion of vorticity into height gradients requires the use of an inverse balance operator which is very ill-conditioned in the vicinity of the equator. An non-zero height gradient in this area is not physically absurd, because any reasonable perturbation of the vorticity equation model state will be perpendicular to it, i.e., there can be no height gradient near the equator under the strict geostrophic hypothesis. Such a gradient field is undesirable, though, because it does not provide any useful information, so we have chosen to represent it in the streamfunction space where the metric is more appropriate. This little difficulty, common to most applications of adjoint techniques for sensitivity studies, is very similar to the use of the adjoint of normal mode initialization for a primitive-equation models in Rabier et al. (1993).

The integration of H_i^{T} by the adjoint model contains all the useful dynamics for the variance prediction. It yields the gradient of the predicted value of i with respect to the initial state, whose grid-point values may be regarded as the local sensitivity of the prediction of i to any initial perturbation Y, because

$$H_i R Y = \langle R^{\mathrm{T}} H_i^{\mathrm{T}}, Y_i \rangle, \tag{15}$$

i.e., the local contribution to the prediction error of i is the product of the local initial error by the local value of $R^{\mathrm{T}} H_i^{\mathrm{T}}$. The effect of the adjoint integration is sensitive to the trajectory, so that it will be examined for several flows in the following sections.

The product by the matrix S amounts to multiplying the gradient at each point by the initial r.m.s. error field, i.e., the dynamical sensitivity is taken into account only in the areas where there is a significant uncertainty on the initial state. This makes the method more realistic than previous predictability studies which relied solely on the determination of the most unstable modes of the dynamical model: here, the structure of the initial uncertainty is considered. With our simple initial condition, the structure of the diagonal of S is the zonally symmetric height standard deviation already depicted (lower curve of Fig. 2). In streamfunction space, it takes a slightly different form, because of the multiplication by the Coriolis parameter. Its effect here is to avoid giving too much importance to gradient fields near the equator. The streamfunction standard deviation near the equator is equal to $1.8 \cdot 10^6\,\mathrm{m}^2\,\mathrm{s}^{-1}$. It would be possible to take a much more realistic field to account for heterogeneities in the observation network, without increasing the computational cost.

The product by the "square-root" matrix T yields a field where each grid-point value is the inner product of the corresponding row of T with the field $SR^{\mathrm{T}} H_i^{\mathrm{T}}$. This may be quite difficult to interpret if the rows of T are complicated, depending on the complexity of C. If the correlations in P_0 are homogeneous and isotropic, T has a simple form because C is diagonal in spectral space (Gauthier et al., 1993). In grid-point space, the coefficients of its rows depend only on the distance

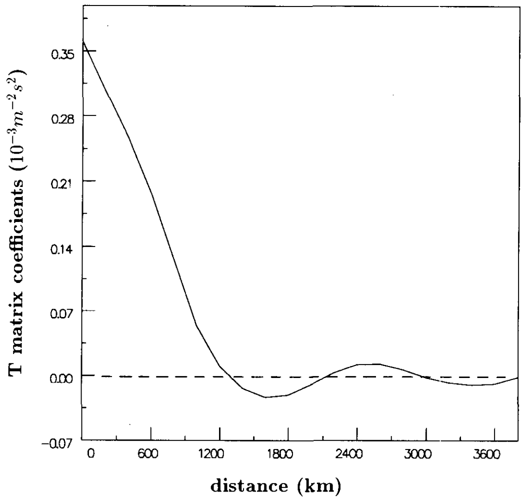

Fig. 7. Repartition of the coefficients of the square-root matrix T with distance.

from the grid point defining each row; with our gaussian correlation model, the dependence on distance is shown in Fig. 7, which is roughly gaussian with approximately the same influence radius as in the correlation model. Multiplying a field by such a matrix amounts to a spatial low-pass filtering, with a cutoff wavelength of about 900 km. In other words, only the largest structures of the sensitivity fields $SR^{\mathrm{T}} H_i^{\mathrm{T}}$ will be considered to contribute to the uncertainty of the prediction. The assertion that only large-scale error structures are likely to occur in the analysis is directly related to the choice of the initial correlations, and its realism remains to be discussed.

Lastly, the structure of the field $TSR^{\mathrm{T}} H_i^{\mathrm{T}}$ gives the mapping of the contribution of the initial state uncertainty to the final error standard deviation. If a covariance $\mathrm{cov}(i, j)$ is to be computed, the local contributions to it are given by the grid-point product of the corresponding fields $TSR^{\mathrm{T}} H_i^{\mathrm{T}}$ and $TSR^{\mathrm{T}} H_j^{\mathrm{T}}$. We are now going to concentrate on the effects of the dynamics on standard error prediction.

5. Results

In this section, the evolution of local forecast error variances is examined for simple atmospheric flows, using the decomposition of the forecast equation which had been depicted above.

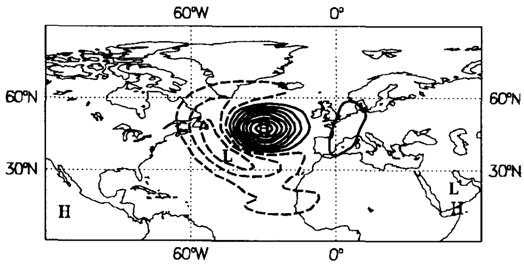

Fig. 8. Gradient of the 24-h height prediction at (45° N, 35° W) with respect to the initial condition, in streamfunction space, with a "state of rest" trajectory. The unit is m^{-1} s, the interval is $2 \cdot 10^{-7}$.

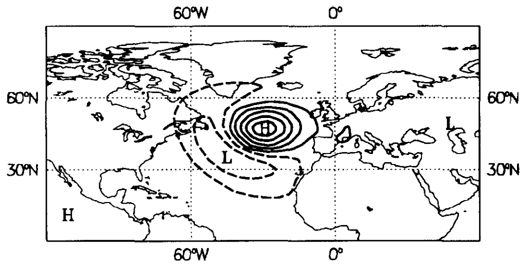

Fig. 10. Field obtained by multiplying the gradient field in Fig. 10 by a square root of the initial error matrix. The canonical norm of this field is equal to the forecast height standard deviation at (45° N, 35° W) (m). The interval is 1.

5.1. Rest state and superrotation

In this experiment, the reference trajectory is the state of rest on the sphere, the adjoint interpolator H_i^T on the reference point (45° N, 35° W) is the one depicted in Section 4. The result $R^T H_i^T$ of the adjoint integration on 24 h is shown in Fig. 8. There is a large positive sensitivity on the reference point, which means that an initial perturbation will tend to remain at the same place during 24 h. There is also an area of negative sensitivity to the SW of the reference point. The phenomenon at hand is made more visible on Fig. 9 where the adjoint integration has been extended over 72 h. It shows a wavetrain propagating southeastwards along a great circle. This is very similar to the response of a linearized vorticity equation model to a localized vorticity source (see Fig. 3 in Branstator, 1983), except the Rossby wave propagation takes place towards the west. An examination of the tangent linear and adjoint vorticity equation (Talagrand and Courtier, 1987) shows that these two models actually contain the same dynamics when the basic state is the state of rest, but since the adjoint integration takes place backwards in time, it is equivalent to inverting the Earth rotation, i.e., the west and the east are swapped. As a consequence, a positive local perturbation to the initial streamfunction will tend to produce negative height forecast errors on the northeast of it 24 h later.

The multiplication of the 24-h gradient by TS yields the field shown in Fig. 10. It is very similar to the gradient field itself; its norm is the forecast error standard deviation: 14.9 m against 16.5 m initially. This is an effect of diffusion, which damps the initial errors, thus reducing the uncertainty of the predicted state. The relative reduction of the initial standard deviations is almost uniform on the sphere. The forecast autocorrelation field, with the same reference point, is shown in Fig. 11. Although it involves more information than the previous field, it is interesting to notice a weak negative correlation on the SW, which corre-

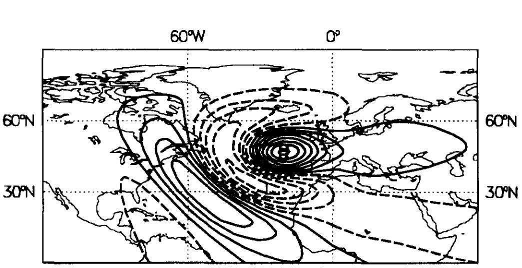

Fig. 9. Same as for Fig. 10, but for a 72-h prediction. The interval is 10^{-7}.

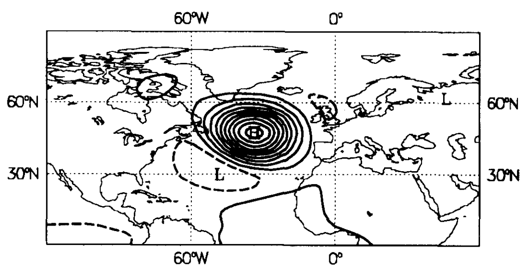

Fig. 11. Autocorrelation of the 24-h forecast height error field at (45° N, 35° W), with a "state of rest" trajectory. The interval is 0.1 with the highest isoline at 0.95.

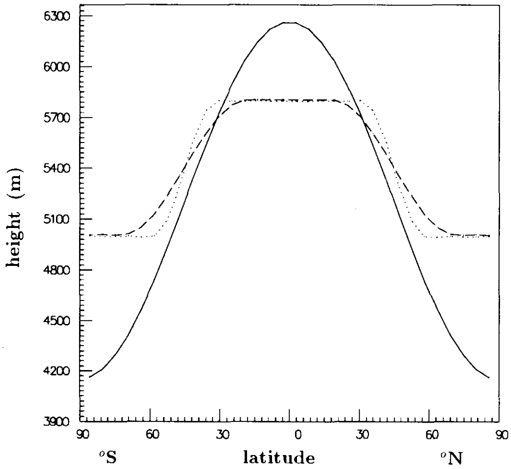

Fig. 12. Latitudinal height structure of the three zonal fields used in the experiments. Heavy curve: superrotation; dashed and dotted curves: first and second "zonal jet" experiments, respectively.

sponds to the northeastwards propagation of initial errors, as explained above.

When the reference trajectory is built as a solid body rotation state, or superrotation, the corresponding height field is zonal and stationary with the structure shown in Fig. 12 (heavy curve). The results are identical to the rest state, with the gradient field shown on Fig. 13, except for a westward shift upstream of the reference point, because the adjoint of the advection is the advection in the reverse direction. In other words, the errors are advected by the basic flow.

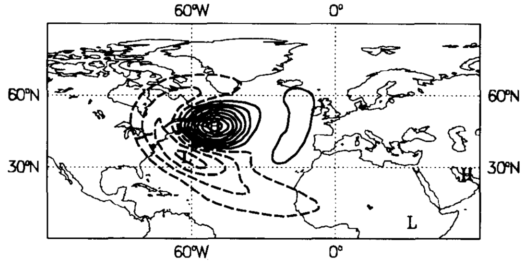

Fig. 14. Gradient of the 24-h height prediction at (45° N, 35° W) in the first "zonal jet" experiment, in streamfunction space. The interval is $2 \cdot 10^{-7}$.

5.2. *Zonal jets*

A somewhat more meteorological trajectory consists of a couple of zonal jets, one in each hemisphere, with sine latitudinal wind profiles. In a first experiment, the maximum speed is set to 20 m s^{-1}. The latitudinal structure of the corresponding height field is shown on Fig. 12 (dashed curve). The gradient of the height prediction is shown on Fig. 14. It is only slightly different from the previous ones, with a deformation of the negative sensitivity area which is perhaps attributable to Rossby waves refraction (Hoskins and Karoly, 1981). The forecast variances are still almost uniform but the damping is slower than in the previous experiment.

In a second experiment, the maximum speed is set to 40 m s^{-1}, so that the jets are barotropically unstable: the module of the largest eigenvalue of the tangent linear R is 1.33, while it was 0.99 in the former experiment. The latitudinal structure of the height field of the basic state is shown on Fig. 12 (dotted curve). The gradient field Fig. 15 is quite

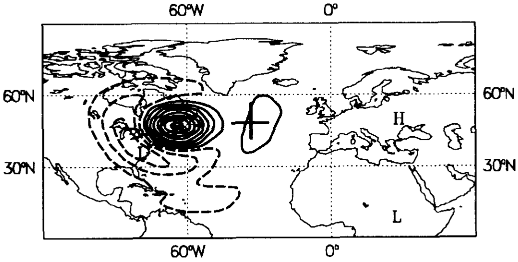

Fig. 13. Gradient of the 24-h height prediction at (45° N, 35° W) in the "superrotation" experiment, in streamfunction space. The interval is $2 \cdot 10^{-7}$. The cross marks the (45° N, 35° W) point.

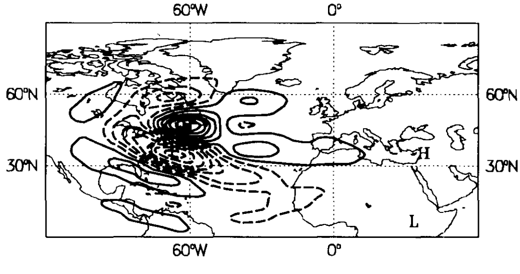

Fig. 15. Gradient of the 24-h height prediction at (45° N, 35° W) in the second "zonal jet" experiment, in streamfunction space. The interval is $3 \cdot 10^{-7}$.

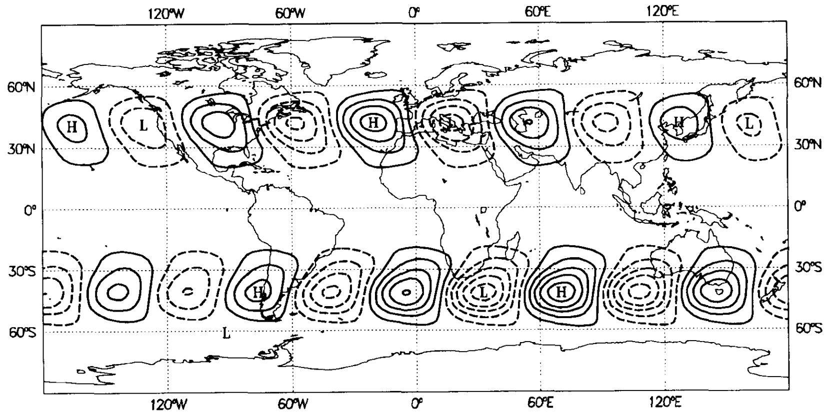

Fig. 16. Streamfunction of the most unstable mode in the second "zonal jet" experiment. The interval is $\frac{1}{10}$ of the maximum amplitude.

different from the previous ones: the scales are smaller, and the amplitude is larger. The forecast error standard deviations are up to 50% larger than in the initial state, particularly in the vicinity of the jets. Thus, the presence of instability in the flow leads to an increase of the forecast uncertainty. The structure of the gradient is tilted against the flow shear, which makes it an efficient initial condition for extracting energy from the basic flow. Actually, this gradient is optimal in a sense we are going to explain and compare with other concepts of optimal error growth.

5.3. Comparison with some optimal modes in the case of unstable zonal jets

In most previous studies, error growth in atmospheric models was studied using the most unstable modes of the flows, i.e., the largest eigenvectors (in module) of the resolvent R. The structure of the most unstable mode $X_{\max}$ of the $40\ \mathrm{m\,s^{-1}}$ jet flow is shown in Fig. 16. It has the structure of a linear barotropic wave along the jet, with a definite wavelength resulting from local barotropic instability conditions and from constraints related to the spherical geometry. This

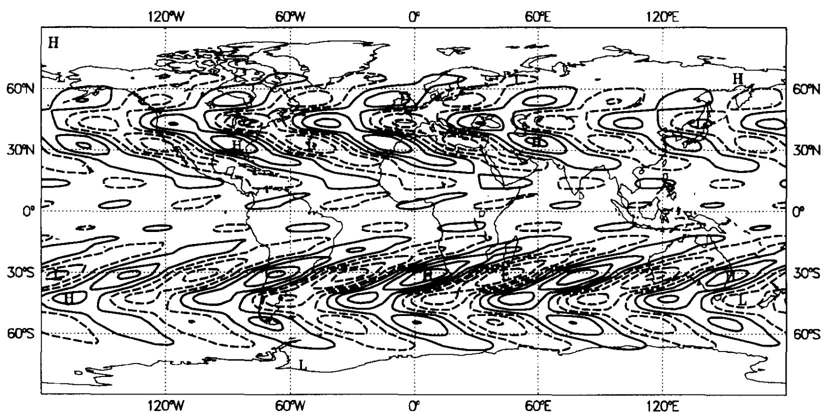

Fig. 17. Streamfunction of the initial condition which yields the largest projection onto the most unstable mode after a 24-h integration, in the second "zonal-jet" experiment. The interval is $\frac{1}{6}$ of the maximum amplitude.

field defines the initial perturbation of the tangent linear model with the largest growth rate at time goes to infinity.

It is possible, however, to find an initial perturbation with an even larger growth rate on a finite time interval (Farrel, 1988): The vector $R^{\mathrm{T}}X_{\max}$, which yields the largest projection onto $X_{\max}$ after the integration, has usually a larger growth rate than $X_{\max}$ itself as long as the model R is not self-adjoint (Borges and Hartmann, 1992; Farrel and Moore, 1992). The structure of this vector, shown in Fig. 17, is quite different from that of $X_{\max}$, and is locally very similar to that of Fig. 15.

The gradient field $R^{\mathrm{T}}H_i^{\mathrm{T}}$ is optimal in the following sense: find an initial perturbation Y of fixed norm such that the absolute value of the perturbation on the forecast of i is maximal. This can be written as

$$\max_{Y,\, \|Y\| \text{ fixed}} |H_i R Y|. \tag{16}$$

Following the Cauchy–Schwartz inequality, the following relationships hold:

$$|H_i R Y| = |\langle R^{\mathrm{T}} H_i^{\mathrm{T}}, Y \rangle| \tag{17}$$

$$\leqslant \|R^{\mathrm{T}} H_i^{\mathrm{T}}\| \, \|Y\|, \tag{18}$$

which shows that, since the norms of $R^{\mathrm{T}}H_i^{\mathrm{T}}$ and Y are fixed, the optimum is reached when there is an equality in the above expression, i.e., the solution to the problem is that Y is proportional to $R^{\mathrm{T}}H_i^{\mathrm{T}}$. Thus, the gradient field defines an optimal perturbation of the parameter of interest. It is instructive to integrate this gradient with the tangent linear model, so that the meaning of the gradient structure is made more apparent. Fig. 18 shows this integration for 48 h, bearing in mind that the perturbation is optimal for the height at (45° N, 35° W), marked by a cross in panel (a), only for the 24 h range (panel (c)). The perturbation undergoes a strong amplification during the first 24 h as its tilt is reduced by the jet shear. Then it takes the form of a wave packet propagating downstream, with a local wavelength very similar to that of the normal mode (Fig. 16). There is an interesting similarity between the forecast autocorrelation function, in Fig. 19, and the 24-h optimal mode forecast in panel (c) of Fig. 18, which is equivalent to a forecast error autocorrelation function with an initial matrix P_0 equal to identity. It shows that, with our simple initial condition, the correlations are mainly determined by the dynamics alone, while the specification of the matrix P_0 is important for the forecast of the variances.

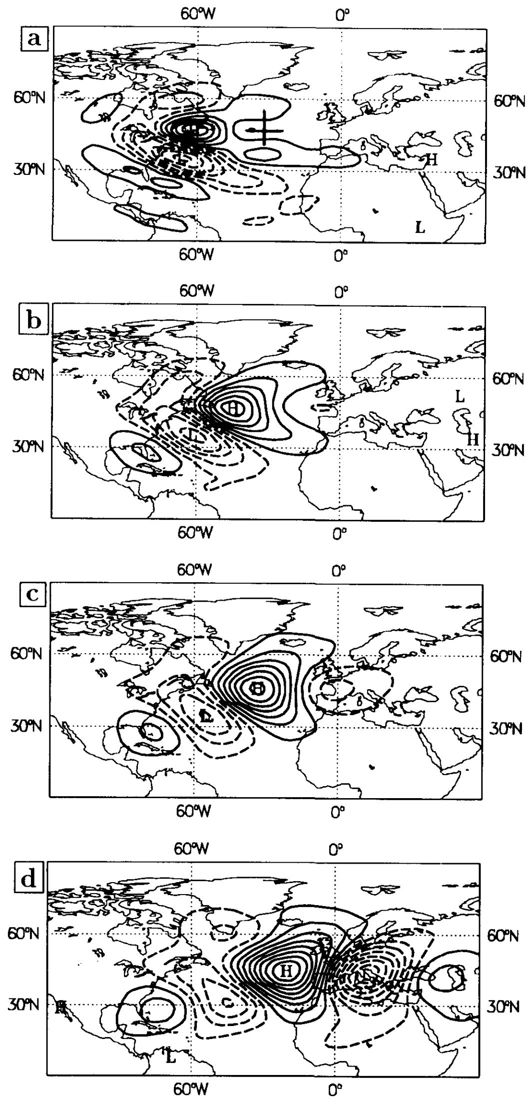

Fig. 18. Integration of the gradient field in the right-hand panel of Fig. 16, using the tangent linear model of the second "zonal jet" experiment. The evolution of the streamfunction is represented at times 0, 12, 24, 48 in panels (a), (b), (c), (d) respectively. The cross in panel (a) marks the (45° N, 35° W) point. The interval in each panel is $\frac{1}{10}$ of the maximum amplitude.

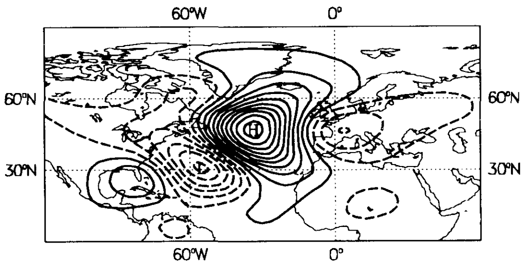

Fig. 19. Autocorrelation of the 24-h forecast height error field at (45° N, 35° W), with the second "zonal jet" experiment. The interval is 0.1 with the highest isoline at 0.95.

5.4. *Non-zonal flows*

So far, we have considered only zonal flows. In the real large-scale atmosphere there are locally strong zonal variations of the jets, both in strength and in direction. In Fig. 20a, an equatorially symmetric initial condition has been built as an alternance of weak and strong westerlies, as in the atmospheric climatology. It is symmetric with respect to the equator and invariant under a longitude shift of 120 or 240 degrees. The trajectory computed by the vorticity model is not more stationary, nevertheless its evolution is rather slow during the first 24 h. The mapping of the forecast r.m.s. error field on the Northern hemisphere is shown in Fig. 20b. As in Fig. 3, there are localized areas of enhanced r.m.s. error growth in the midlatitudes. They are found in the diffluence regions, which could be thought as linked to strong kinetic energy conversion into the perturbations, following some previous works (Hoskins et al., 1983). However, additional experiments have shown that this is not the case, at least which such a simple basic state: reconducting the experiment with larger zonal extensions of the fast and slow parts of the jet has shown that the forecast variances are not larger in the jet exit regions than in the fast parts of the jet. The variances are larger where the jet is faster because, as we have seen, there is local error growth linked to barotropic instability in these areas. The downstream shifting of the maximum standard deviations relative to the fast parts of the jet is simply due to the advection by the basic flow.

Its has been suspected in Section 3 that the position of large-scale troughs and ridges may be important in focusing the variance growth on par-

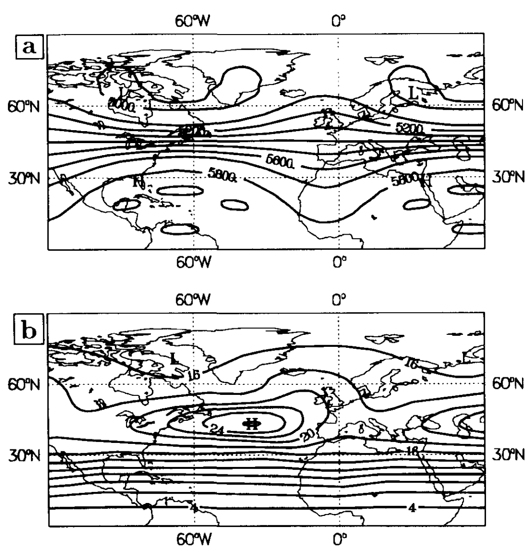

Fig. 20. (a) height field defining the initial condition for the trajectory in the first "non-zonal flow" experiment, in meters; (b) predicted height error standard deviations after 24 h in the first "non-zonal flow" experiment (m).

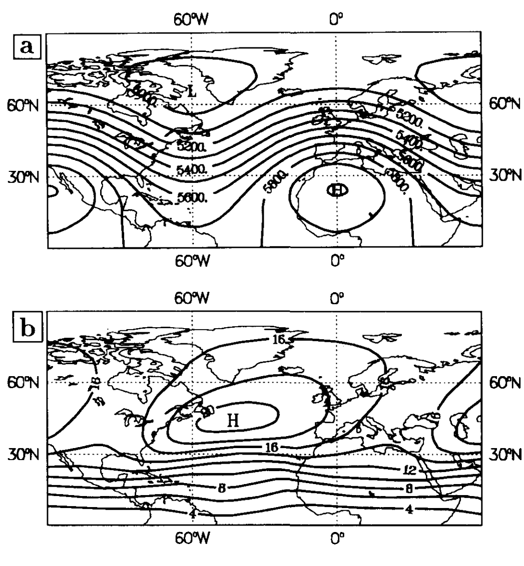

Fig. 21. (a) height field defining the initial condition for the trajectory in the second "non-zonal flow" experiment, in meters; (b) predicted height error standard deviations after 24 hours in the second "non-zonal flow" experiment, in meters.

ticular areas. In Fig. 21a, an initial state has been built as an equatorially symmetric, undulating jet without significant wind speed variations along it. Its symmetries are the same as in the former state. The subsequent trajectory is almost stationary. The forecast standard deviations are shown on Fig. 21b. There are once again large local increases of the standard deviation, and the maxima are centered on the eastern flanks of the troughs. In a recent paper, Barkmeijer (1992) found very similar results with a simpler error covariance model. Though the standard deviation patterns are strikingly close to those in Section 3, a better understanding of the phenomenon at hand should be sought, presumably using detailed energy conversion diagnostics as in Simmons et al. (1983).

5.5. *Generalization to real flows*

In the previous experiments, some very large scale flows have been designed in order to mimic some features of the more realistic T21 analysis on Fig. 1. Whether conclusions made on such flows may be generalized, though they do not take into account small scale features, remains to be seen. To get some confidence on this point, an experiment has been designed in which the trajectory is filtered in spectral space to total wavenumber 10. The corresponding initial state is shown in

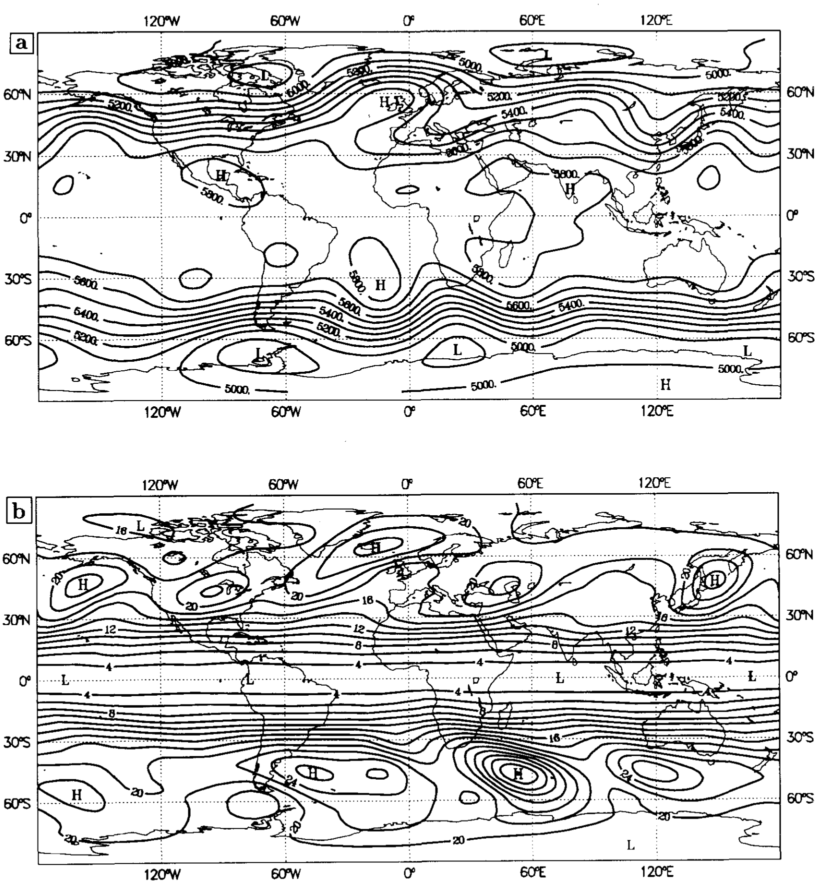

Fig. 22. (a) 500 hPa geopotential height analysis from ECMWF, on 1 December 1990, 00 UTC, at T10 triangular spectral truncation (m); (b) predicted height error standard deviations after 24 h with the same conditions as in the first experiment, except the initial condition for the trajectory is spectrally truncated at T10.

Fig. 22a: it contains only the largest features of Fig. 1, while smaller ones, like the cutoff low on the Azores and the trough off North America's East Coast, have been erased. The resulting r.m.s. error predicted after 24 h is shown in Fig. 22b. There is a good qualitative agreement with Fig. 3, particularly with respect to the locations and relative values of the local maxima in midlatitudes. Of course, there is a strong weakening of the overall error prediction, because the filtering process has weakened the jets, reducing the likelihood of local instability. Nevertheless, it seems reasonable to generalize the conclusions on the former flows to more complicated barotropic situations.

6. Summary and discussion

Starting from a very simple initial condition and neglecting model errors, a global vorticity equation model is able to produce some information on the forecast probability density function which is related to the dynamics of the flow. Even for quite short ranges, there are some modifications of the error variances and correlations. Taking into account those modifications in practice would be interesting for accurately assessing the guess-field errors in analysis methods (variational assimilation as well as OI). They are important for predictability studies, too. However, the prediction of the second-order error moments of the whole flow is computationally very expensive, so that more economical methods have to be found for the application to realistic models. To achieve this, it is necessary to understand the mechanisms by which covariances evolve. This is possible with our simple model, using an appropriate decomposition of the covariance prediction equation, where the effects of initial variances and correlations and of the model dynamics can be interpreted separately.

The effects of the dynamics for local variance (and equivalently, covariance) prediction are shown to reduce to the study of the adjoint integration of an appropriate interpolation operator, which yields the mapping of the sensitivity of a local prediction to the initial errors. The application to simple academic flows reveals how hydrodynamic concepts are relevant to the forecast of forecast skill: the initial errors undergo a dispersion mechanism which is constrained by the dynamics of Rossby waves on the sphere; the diffusion in the model has an effect in reducing the effect of the initial errors, at least in trivial flows; the initial errors tend to be advected downstream by the basic flow; the presence of local barotropic instabilities, particularly in the regions of strong shear, leads to a rapid amplification of the uncertainty on the model state. Additionally, it is shown that the effects of non-zonal features of the large-scale flow patterns are important and should be studied in more details. A thorough understanding of the evolution of variances and correlations in such academic flows, when carried out, may provide a good basis to understand the mechanisms of error prediction in more realistic flows.

Of course, we have so far studied only large-scale barotropic flows on short ranges. The effects of baroclinic instability need to be assessed. Much work remains to be done for a realistic specification of the initial error condition. As we have shown, the usual choice of an homogeneous isotropic gaussian structure for the analysis amounts to excluding the possibility of small-scale errors, which is obviously unrealistic since there may be a significant amount of energy in scales unresolved by the analysis. This problem should be studied with higher-resolution models, and will probably be solved by an accurate parameterization of small-scale errors as in Pitcher (1977). A similar difficulty is likely to arise in baroclinic studies, because the usual vertical separation hypothesis for the correlations in operational OI does not favour the development of baroclinic structures (Veyre, 1991). A definite solution is certainly in the implementation of some simplified form of the Kalman filter, so that the initial condition for the error matrix follows naturally from the former forecasts and analyses. Lastly, specific studies should be made on the statistical structures of the model error noise.

Nevertheless, some applications of this work can already be explored. From the identification of the dynamical processes leading to variance evolution, it is possible to design an empirical model in which analysis error variances would be advected by the flow and modified by simple "physical" parameterizations, e.g., to account for local growth when local conditions for instability are verified. A similar work can be done for the correlation structures. Another more precise approach is to take advantage of the fact that gradient structures, as we have defined them, tend to be local in space, or equivalently that the group velocity of the errors is limited. It means that the resolvent of the adjoint model has a kind of band structure in physical space. Similarly to Parrish and Cohn (1985), it may form the basis of an economical method for the integration of the error matrix forecast equation, so that a computational factor of at least 10 could be gained. The design of such a method will be undertaken in the near future.

7. Acknowledgements

The author thanks O. Talagrand and J. Pailleux who both supervised this study, and P. Veyre for useful suggestions. This work is partially supported by the Centre National de la Recherche Scientifique, Groupement de Recherche "Méthodes Variationnelles en Météorologie et Océanographie".

REFERENCES

Barkmeijer, J. 1992. Local error growth in a barotropic model. *Tellus 44A*, 314–323.

Barkmeijer, J. and Opsteegh, J. D. 1991. Local skill prediction with a simple model. *Proc. 1991, ECMWF Workshop on New developments in predictability.* ECMWF, Shinfield Park, Reading, UK.

Borges, M. D. and Hartmann, D. L. 1992. Barotropic instability and optimal perturbations of observed nonzonal flows. *J. Atmos. Sci. 49*, 335–354.

Branstator, G. 1983. Horizontal energy propagation in a barotropic atmosphere with meridional and zonal structures. *J. Atmos. Sci. 40*, 1689–1708.

Cohn, S. E. and Parrish, D. F. 1991. The behavior of forecast error covariances for a Kalman filter in two dimensions. *Mon. Weather. Rev. 119*, 1757–1785.

Courtier, P., Freydier, C., Geleyn, J.-F., Rabier, F. and Rochas, M. 1991. The ARPEGE Project at Météo-France. *Proc. 1991, ECMWF Seminar*, September 1991. ECMWF, Shinfield Park, Reading, UK.

Dee, D. P. 1991. Simplification of the Kalman filter for meteorological data assimilation. *Mon. Weather. Rev. 117*, 365–384.

Epstein, E. S. 1969. Stochastic dynamic prediction. *Tellus 21*, 739–759.

Farrel, B. F. 1988. Optimal excitation of neutral Rossby waves. *J. Atmos. Sci. 45*, 163–172.

Farrel, B. F. and Moore, A. M. 1992. An adjoint method for obtaining the most rapidly growing perturbation to oceanic flows. *J. Phys. Oceanog. 22*, 338–349.

Gauthier, P., Courtier, P. and Moll, P. 1993. Data assimilation with an extended Kalman-Bucy filter. *Mon. Weather. Rev. 121*, in press.

Ghil, M. 1989. Meteorological data assimilation for oceanographers. Part I: description and theoretical framework. *Dyn. of Atm. and Oceans 13*, 171–218.

Ghil, M., Cohn, S., Tavantzis, J., Bube, K. and Issacson, E. 1981. Applications of estimation theory to numerical weather prediction. In: *Dynamic meteorology. Data assimilation methods.* (Eds. Bengtsson, L., Ghil, M. and Källén, E.) Springer-Verlag, New York, 139–224.

Hollingsworth, A. and Lönnberg, P. 1986. The statistical structure of short-range forecast errors as determined from radiosonde data. Part I: The wind field. *Tellus 38A*, 111–136.

Hoskins, B. and Karoly, D. 1981. The steady linear response of a spherical atmosphere to thermal and orographic forcing. *J. Atmos. Sci. 38*, 1179–1196.

Hoskins, B., James, I. and White, G. 1983. The shape, propagation and mean-flow interaction of large-scale weather systems. *J. Atmos. Sci. 40*, 1595–1612.

Lacarra, J.-F. and Talagrand, O. 1988. Short-range evolution of small perturbations in a barotropic model. *Tellus 40A*, 81–95.

Lönnberg, P. and Hollingsworth, A. 1986. The statistical structure of short-range forecast errors as determined from radiosonde data. Part II: the covariance of height and wind errors. *Tellus 38A*, 137–161.

Lorenc, A. C. 1986. Analysis methods for numerical weather prediction. *Q. J. R. Meteorol. Soc. 112*, 1177–1194.

Palmer, T. N. and Tibaldi, S. 1987. *Predictability studies in the median and extended range.* ECMWF Technical Memorandum no. 139. ECMWF, Shinfield Park, Reading, UK.

Parrish, D. F. and Cohn, S. E. 1985. *A Kalman filter for a two-dimensional shallow-water model: formulation and preliminary experiments.* NMC Office note no. 304. National Meteorological Center, Washington DC, USA.

Pitcher, E. 1977. Application of stochastic dynamic prediction to real data. *J. Atmos. Sci. 34*, 3–21.

Rabier, F., Courtier, P. and Talagrand, O. 1993. An application of adjoint model to sensitivity analysis. *Contributions to Atmospheric Physics.*

Simmons, A., Wallace, J. and Branstator, G. 1983. Barotropic wave propagation and instability, and atmospheric teleconnection patterns. *J. Atmos. Sci. 40*, 1363–1392.

Talagrand, O. and Courtier, P. 1987. Variational assimilation of meteorological observations with the adjoint vorticity equation. I: Theory. *Quart. J. Roy. Meteor. Soc. 113*, 1311–1328.

Veyre, P. 1991. Direct prediction of error variances by the tangent linear model. *Proc. 1991, ECMWF Workshop on New developments in predictability.* ECMWF, Shinfield Park, Reading, UK.